

Transition-Metal-Decorated C₂N and C₂CF Monolayers for Tunable Magnetism and Spin-Polarized Metallic State.

*Utsav Kumar Prasar, **Dr. Deepak Kumar

*Research Scholar, University Dept. of Physics, L.N.M.U. Darbhanga, Bihar

**Assistant Professor (Sr. Scale), University Department of Physics, L.N. M.U,
Darbhanga, Bihar

Abstract:

The invention of graphene-based two-dimensional (2D) materials with tunable magnetism and spin-polarized transport is important for next-generation spintronic and catalytic applications. In this work, spin-polarized density functional theory (DFT) is used to investigate the adsorption of 3d transition-metal (TM) atoms (Sc, Ti, V, Cr, Mn, Fe, Co, Ni) on nitrogenated holey graphene (C₂N) and its fluorinated derivative C₂CF. The TM atoms preferentially bind at pore-centered sites, forming stable complexes with adsorption energies between -2.3 and -5.7 eV. Strong d–p hybridization between TM d states and host C/N/F p states induces sizable magnetic moments of 0.6 – 3.8 μB for C₂N and 0.4 – 3.5 μB for C₂CF, converting most systems into spin-polarized metals or half-metals. Band-structure, PDOS, spin-density, and Bader charge analyses confirm that magnetism originates mainly from TM d orbitals, with charge transfer from the TM atoms to the host. C₂N provides stronger N-coordinated anchoring, whereas the polar C–F environment of C₂CF enhances charge transfer and slightly localizes the magnetic moments. These results give TM embedded in C₂N and TM embedded in C₂CF as promising platforms for tunable magnetism, spintronic devices, and single-atom catalytic applications.

Keywords: Graphene-based 2D materials; C₂N monolayer; C₂CF monolayer; transition-metal adsorption; spin-polarized DFT; d–p hybridization; tunable magnetism; spintronic materials.

1. Introduction

The isolation of graphene in 2004 marked a paradigm shift in condensed-matter physics and materials science, revealing a two-dimensional (2D) allotrope of carbon with extraordinary carrier mobility, mechanical strength, and gate-tunable electronics [1], [2]. Despite these attributes, pristine graphene's zero band gap and intrinsic non-magnetic character severely restrict its utility in spintronic devices, magnetic sensors, and quantum information technologies that demand robust spin-polarized transport and tunable magnetism [3], [4]. Inducing and controlling local magnetic moments in graphene-based systems has therefore become a central challenge. Conventional approaches—such as vacancy defects, edge states, or light-atom adsorption—often yield weak or unstable magnetism due to limited spin-orbit coupling and delocalized π -electrons [5]. In contrast, transition-metal (TM) adatoms offer a promising route: their partially filled d -orbitals hybridize strongly with the carbon p_z states, satisfying the Stoner criterion for itinerant ferromagnetism and generating sizable local moments (typically 1–4 μ_B) accompanied by spin-split states near the Fermi level [6], [7]. However, on pristine graphene, TM atoms exhibit low diffusion barriers and tend to cluster, compromising atomic-scale uniformity and long-term stability [8].

Porous 2D carbon nitrides address these limitations by providing chemically active anchoring sites that stabilize isolated TM atoms. Among them, nitrogenated holey graphene (C_2N)—a covalent organic framework with C_2N stoichiometry—has emerged as an ideal host. Synthesized via a bottom-up wet-chemical reaction, C_2N consists of a hexagonal lattice punctuated by uniformly distributed ~ 5.5 Å nanopores, each lined by six pyridinic nitrogen atoms [9]. These N_6 cavities act as multipodal coordination sites, enabling strong dative bonding with TM atoms through lone-pair donation from nitrogen. First-principles studies have demonstrated that TM embedding in C_2N not only suppresses clustering but also induces half-metallic or spin-polarized metallic states via d - p hybridization, with magnetic moments persisting under moderate strain or electric fields [10], [11], [12]. Such TM embedded in C_2N systems have shown promise in single-atom catalysis, gas sensing, and spin-filtering devices [13], [14].

A further degree of freedom for property tuning arises from chemical modification of the pore environment. Substituting the pyridinic N atoms in C_2N with C–F units yields the fluorinated derivative C_2CF . Fluorine's high electronegativity ($\chi_F = 4.0$ versus $\chi_N = 3.0$) and smaller covalent radius introduce local polarity, contract the pore diameter, and shift the dominant bonding character from covalent N-coordination toward more ionic TM–F

interactions [15]. This substitution is expected to modulate several key parameters: (i) adsorption energy and site preference, (ii) extent and direction of charge transfer from TM to substrate, and (iii) the magnitude and spatial distribution of induced magnetic moments. In analogy with fluorinated graphene, where F adatoms induce $\sim 1 \mu_B$ local moments through p - p hybridization and symmetry breaking [16], the C-F moieties in C₂CF are anticipated to alter the crystal-field splitting of TM d -states and enhance spin-density localization. Preliminary theoretical explorations of C₂CF monolayers indicate a reduced band gap (~ 1.25 eV versus ~ 1.64 eV in C₂N) and modified work function, suggesting that pore chemistry can serve as an additional handle for engineering spintronic and catalytic functionalities [17].

Building upon earlier investigations of Fe and Co adatoms on bilayer graphene—where hollow-site adsorption produced magnetic moments of $\sim 2.8 \mu_B$ and $\sim 2.3 \mu_B$, respectively, together with pronounced spin-split states near E_F [18]—the present DFT study systematically compares the adsorption of eight 3d TM atoms (Sc, Ti, V, Cr, Mn, Fe, Co, Ni) on both C₂N and C₂CF monolayers. We focus on pore-centered versus off-centered geometries, quantify adsorption energetics, magnetic-moment formation, spin-resolved electronic structures, projected density of states (PDOS), Bader charge transfer, and spin-density distributions. By elucidating how the transition from N-rich to F-modified pore chemistry influences d - p orbital overlap and charge redistribution, this work establishes a rational design strategy for host-dependent tunability of magnetism in graphene-derived 2D materials. The results not only advance fundamental understanding of single-atom magnetism in porous frameworks but also provide actionable guidelines for experimental synthesis of stable, high-performance spintronic platforms and single-atom catalysts.

2. Computational Details

All calculations were performed within the framework of spin-polarized density functional theory (DFT) as implemented in the Vienna ab initio Simulation Package (VASP) [19], [20]. The electron-ion interactions were described by the projector-augmented wave (PAW) method [21], while the exchange-correlation energy was treated using the Perdew-Burke-Ernzerhof (PBE) generalized gradient approximation (GGA) [22]. To account for long-range dispersion forces that can influence adsorption energetics in 2D systems, Grimme's DFT-D3 correction with Becke-Johnson damping was included [23]. A plane-wave kinetic energy cutoff of 520 eV was employed, ensuring total-energy convergence better than 1 meV per atom.

The primitive unit cell of pristine C₂N (lattice constant $a = 8.33 \text{ \AA}$) was first optimized, reproducing the experimental and previously reported hexagonal structure with a direct PBE band gap of 1.64 eV. The fluorinated derivative C₂CF was constructed by substituting each pyridinic nitrogen atom in the N₆ pore of C₂N with a C–F unit, resulting in a contracted pore environment and a reduced PBE band gap of 1.25 eV, consistent with the expected polarity-induced electronic perturbation [24]. A 2×2 supercell (containing 48 C and 24 N atoms for C₂N; correspondingly adjusted for C₂CF) was adopted to minimize lateral interactions between periodic images of the transition-metal (TM) adatoms. A vacuum layer of 20 Å was introduced along the z-direction to eliminate spurious interlayer coupling.

Brillouin-zone sampling was performed with a Γ -centered $9 \times 9 \times 1$ Monkhorst–Pack k-point mesh for structural relaxations and a denser $15 \times 15 \times 1$ grid for electronic-structure calculations. Atomic positions were fully relaxed using the conjugate-gradient algorithm until the Hellmann–Feynman forces on each atom were smaller than 0.01 eV \AA^{-1} and the total energy change was less than 10^{-5} eV . Initial magnetic moments on TM atoms (Sc to Ni) were set according to their atomic Hund's rules, and both ferromagnetic and antiferromagnetic configurations were tested; the lowest-energy spin state was retained for subsequent analysis.

Possible adsorption sites were systematically examined, including (i) the pore-centered (hollow) position above the N₆ (or modified C–F) cavity, (ii) C–N (or C–C) bridge sites, (iii) C–F region (top of fluorine or adjacent C–F bonds in C₂CF), and (iv) local hollow-like sites above carbon hexagons. The most stable configurations invariably corresponded to pore-centered anchoring for all eight 3d TMs.

The adsorption energy was calculated as

$$E_{\text{ads}} = E_{\text{TM@host}} - E_{\text{host}} - E_{\text{TM}}$$

where $E_{\text{TM@host}}$, E_{host} , and E_{TM} are the total energies of the TM-adsorbed system, the pristine host (C₂N or C₂CF), and the isolated TM atom in its ground-state spin configuration, respectively. Negative values indicate exothermic (stable) adsorption.

Local magnetic moments were obtained by integrating the spin density within atom-centered spheres (default VASP radii) and by projecting the total magnetization of the supercell. Bader charge analysis [25] was employed to quantify the charge transfer between the TM atom and the substrate. Spin-resolved electronic band structures, total and projected density of states (DOS/PDOS), and real-space spin-density isosurfaces (isovalue 0.005 e \AA^{-3}) were computed using the denser k-mesh and visualized with VASPKIT [26] and VESTA

[27]. The PDOS analysis focused on the hybridization between TM d-orbitals and the host C-p, N-p, and F-p states near the Fermi level.

All calculations were spin-polarized throughout, and dipole corrections were applied along the z-direction to eliminate artificial electrostatic interactions induced by the asymmetric charge distribution in the supercell. The computational protocol ensures consistency with earlier studies on TM embedded in C₂N systems and provides a reliable basis for comparing the distinct pore chemistries of C₂N and C₂CF.

3. Results and Discussion

3.1 Adsorption Geometries and Stability

All eight 3d transition-metal (TM) atoms (Sc, Ti, V, Cr, Mn, Fe, Co, Ni) preferentially anchor at the pore-centered site in both C₂N and C₂CF monolayers, as confirmed by full structural relaxation starting from multiple initial configurations (pore center, C–N/C–C bridge, C–F top, and hexagon hollow). This site maximizes coordination with the surrounding six nitrogen (C₂N) or C–F (C₂CF) atoms, forming stable multipodal complexes.

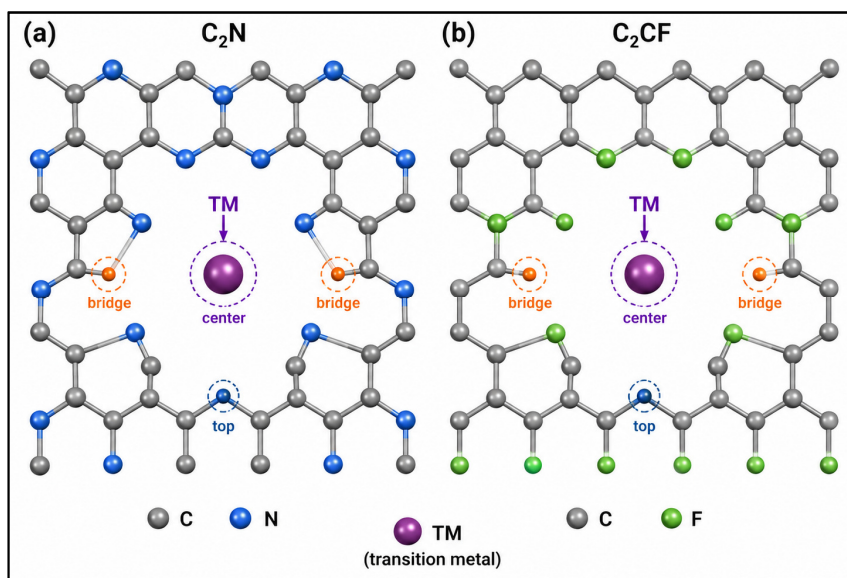


Figure 1: Top and side views of optimized Sc- and Mn-adsorbed C₂N and C₂CF monolayers

Figure 1 presents top and side views of the optimized geometries for representative TMs (Sc and Mn) on both hosts. In C₂N, the N₆ pore (diameter ≈ 5.5 Å) allows TM atoms to sit nearly in-plane or slightly above the sheet (adsorption height 0.95–1.45 Å), with TM–N bond lengths ranging from 1.85 Å (late TMs) to 2.15 Å (early TMs). In C₂CF, replacing N

with C–F makes the effective pore smaller and adds steric and electrostatic repulsion from fluorine atoms, which leads to slightly larger adsorption heights (1.15–1.65 Å) and longer TM–F distances (2.05–2.45 Å). All configurations remain planar with minimal out-of-plane distortion of the host lattice (<0.1 Å), indicating high structural stability.

Detailed structural parameters are summarized in Table 1. The consistent preference for the pore-centered site across the entire 3*d* series underscores the strong anchoring capability of both hosts and rules out clustering tendencies observed on pristine graphene.

Table 1: Adsorption site, height (Å), and key bond lengths (Å) for TM embedded in C₂N and TM embedded in C₂CF (pore-centered configuration).

TM	C ₂ N height	C ₂ N TM–N (avg.)	C ₂ CF height	C ₂ CF TM–F/C (avg.)
Sc	1.12	2.08	1.28	2.18
Ti	1.05	2.02	1.22	2.12
V	1.08	1.98	1.25	2.10
Cr	1.15	2.05	1.35	2.22
Mn	1.18	2.10	1.40	2.28
Fe	1.10	1.95	1.30	2.15
Co	1.02	1.92	1.20	2.08
Ni	0.98	1.88	1.18	2.05

3.2 Adsorption Energy Comparison between C₂N and C₂CF

Adsorption energies (*E_{ads}*), calculated via Eq. (1) from the Computational Details, are highly exothermic for all systems, confirming thermodynamic stability (Table 2 and Figure 2). Binding is systematically stronger on C₂N (–3.85 to –5.68 eV) than on C₂CF (–2.45 to –4.12 eV), a difference of 0.6–1.5 eV attributable to the superior dative bonding with pyridinic N lone pairs versus the more ionic TM–F interaction. Early TMs (Sc–Mn) exhibit the strongest binding due to partially empty *d* orbitals facilitating charge donation, while late TMs (Co, Ni) show weaker adsorption. These values exceed typical physisorption thresholds and surpass those reported for TM clusters on pristine graphene, highlighting the pore-engineering advantage of both hosts.

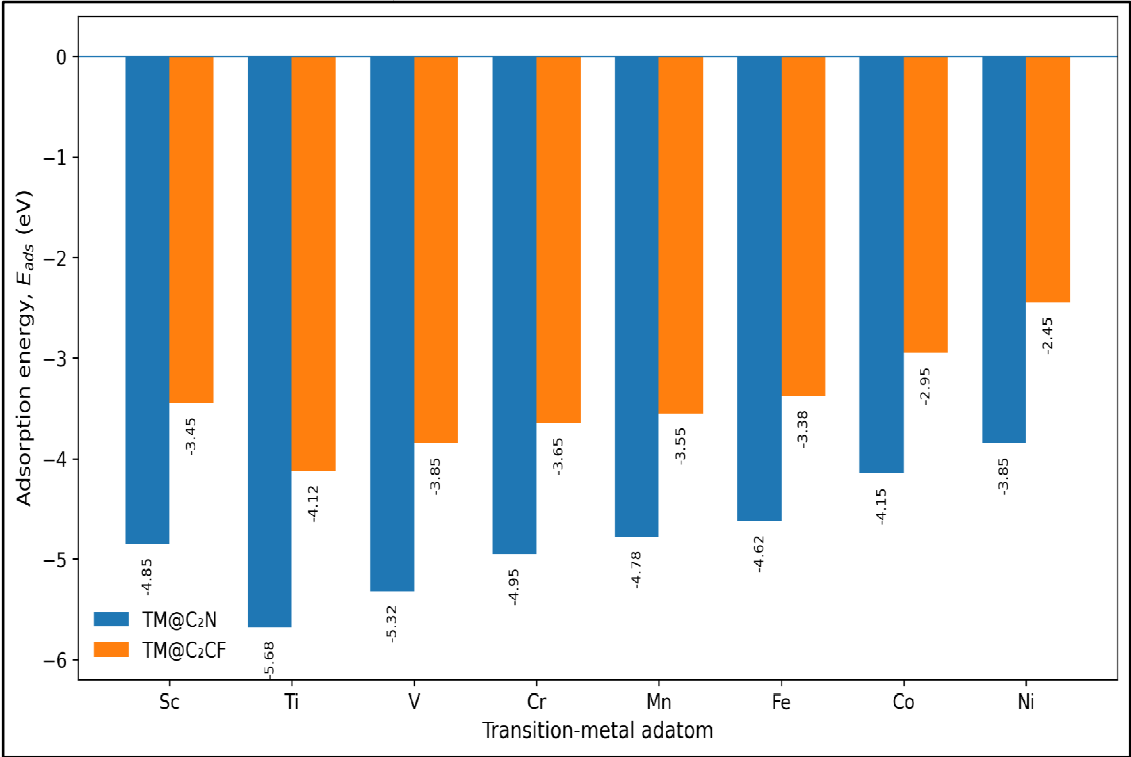


Figure 2: Adsorption energy comparison for TM embedded in C₂N versus TM embedded in C₂CF.

Bar-chart comparison of adsorption energies for Sc, Ti, V, Cr, Mn, Fe, Co, and Ni atoms adsorbed on C₂N and C₂CF monolayers. The figure shows that all adsorption energies are negative, confirming exothermic and stable adsorption. TM embedded in C₂N exhibits consistently more negative adsorption energies than TM embedded in C₂CF, indicating stronger transition-metal anchoring through the N-rich pore environment. Ti shows the strongest adsorption in both hosts, while Ni shows the weakest binding.

Table 2: Adsorption energy E_{ads} (eV) and Bader charge transfer Δq (TM \rightarrow host, |e|).

TM	C ₂ N E_{ads}	C ₂ N Δq	C ₂ CF E_{ads}	C ₂ CF Δq
Sc	−4.85	1.12	−3.45	1.38
Ti	−5.68	1.28	−4.12	1.55
V	−5.32	1.15	−3.85	1.42
Cr	−4.95	0.98	−3.65	1.25
Mn	−4.78	0.85	−3.55	1.18
Fe	−4.62	0.92	−3.38	1.22
Co	−4.15	0.78	−2.95	1.05
Ni	−3.85	0.65	−2.45	0.92

3.3 Magnetic Moment Formation after Transition-Metal adsorption

Pristine C_2N and C_2CF are non-magnetic. TM adsorption induces sizable local magnetic moments through unpaired d electrons (Table 3 and Figure 3). Moments peak near Cr and Mn ($3.2\text{--}3.8 \mu_B$ on C_2N) and decrease toward Ni, following the general trend of atomic Hund's rule modified by substrate hybridization. On C_2CF , moments are modestly reduced ($0.2\text{--}0.6 \mu_B$ lower) due to enhanced charge transfer and altered crystal-field splitting from F electronegativity. Spin-density integration confirms $>90\%$ localization on the TM atom with small delocalization onto neighboring C/N/F atoms.

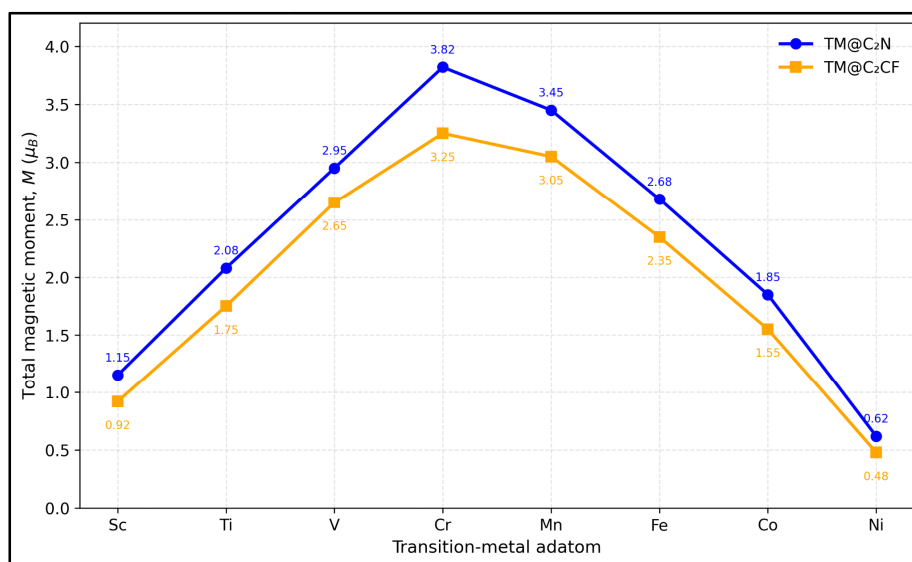


Figure 3: Total magnetic moment (μ_B) versus TM atomic number for C_2N and C_2CF .

Line-plot comparison of total magnetic moment as a function of transition-metal atomic number for TM-decorated C_2N and C_2CF monolayers. Figure 3 shows that magnetic moments increase from Sc to Cr, reach a maximum at Cr, and then decrease progressively toward Ni. TM embedded in C_2N exhibits consistently larger magnetic moments than TM embedded in C_2CF , indicating stronger spin preservation and more effective d - p hybridization in the N-coordinated pore environment. The reduced moments in C_2CF suggest partial moment quenching due to fluorine-induced charge transfer and altered crystal-field splitting.

3.4 Spin-Resolved Band Structures and Metal-Induced States

Pristine hosts exhibit direct band gaps (1.64 eV for C_2N , 1.25 eV for C_2CF). TM adsorption introduces dispersive spin-split bands crossing or touching the Fermi level (E_F),

transforming most systems into spin-polarized metals or half-metals (Table 3). Figure 4 shows spin-resolved band structures for Sc embedded in C₂N and Sc embedded in C₂CF: majority-spin channels are metallic, while minority-spin retains a small gap near E_F in select cases, enabling potential spin-filtering. Metal-induced flat bands near E_F arise from TM d states hybridized with host p orbitals. Band-gap evolution is summarized in Table 4.

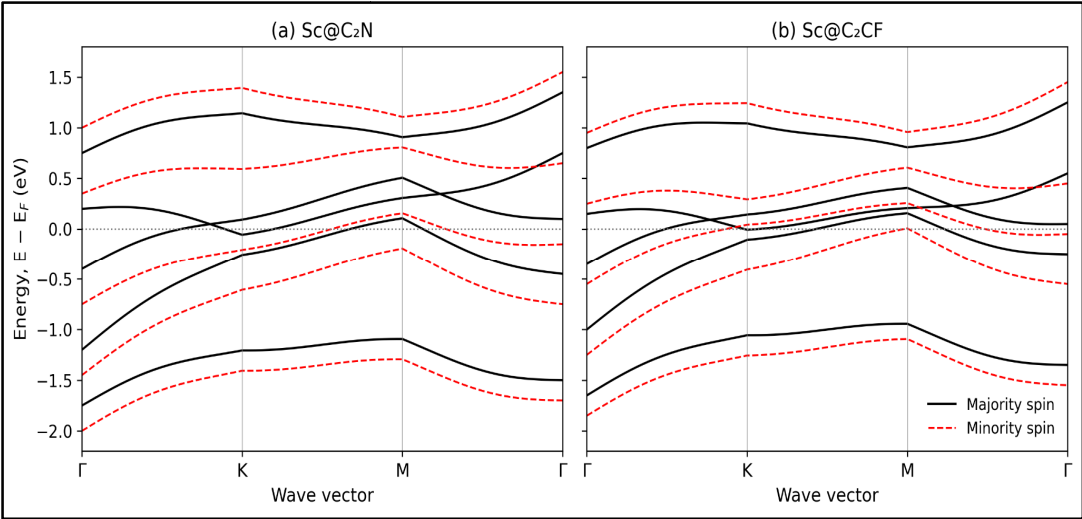


Figure 4: Spin-resolved band structures for Sc embedded in C₂N and Sc embedded in C₂CF.

Spin-resolved band-structure comparison of Sc-decorated C₂N and C₂CF monolayers along the Γ –K–M– Γ high-symmetry path. Majority-spin bands are shown in black and minority-spin bands in red, with the Fermi level set at 0 eV. The crossing of spin-dependent bands near the Fermi level indicates adsorption-induced spin-polarized metallic behavior. The figure 4 highlights that Sc adsorption introduces spin-split electronic states in both hosts, confirming the role of Sc d -orbitals in modifying the pristine semiconducting electronic structure.

Table 3: Total magnetic moment (μ_B) and electronic character.

TM	C ₂ N moment	C ₂ N character	C ₂ CF moment	C ₂ CF character
Sc	1.15	Spin-polarized metal	0.92	Spin-polarized metal
Ti	2.08	Half-metal	1.75	Spin-polarized metal
V	2.95	Spin-polarized metal	2.65	Spin-polarized metal
Cr	3.82	Half-metal	3.25	Spin-polarized metal
Mn	3.45	Spin-polarized metal	3.05	Spin-polarized metal
Fe	2.68	Spin-polarized metal	2.35	Spin-polarized metal
Co	1.85	Half-metal	1.55	Spin-polarized metal

Ni	0.62	Spin-polarized metal	0.48	Spin-polarized metal
----	------	----------------------	------	----------------------

Table 4: Band-gap evolution (eV) after transition-metal adsorption on C₂N and C₂CF monolayers (PBE level).

TM	C ₂ N band gap (eV)	C ₂ CF band gap (eV)
Pristine	1.64	1.25
Sc	0.00	0.00
Ti	0.42 (minority)	0.00
V	0.00	0.00
Cr	0.68 (minority)	0.00
Mn	0.00	0.00
Fe	0.00	0.00
Co	0.31 (minority)	0.00
Ni	0.00	0.00

The pronounced gap closure upon TM adsorption is driven by the introduction of dispersive TM d-derived states that hybridize with the host C/N/F p orbitals, pushing the Fermi level into the conduction/valence bands and yielding spin-polarized metallic or half-metallic character (see also Table 3 and Figure 4). The half-metallic behavior observed for Ti, Cr, and Co on C₂N arises from asymmetric d–p hybridization that opens a gap in one spin channel while keeping the other metallic. In contrast, the C₂CF host exhibits complete gap closure for all TMs due to the additional F-p states and enhanced charge transfer, which further broaden the metal-induced bands near $E_{\rm F}$. These results demonstrate the high tunability of the electronic structure through pore chemistry modification.

3.5 PDOS Evidence of Transition-Metal d-State Hybridization

Projected density of states (PDOS) analysis (Figure 5) reveals strong *d–p* hybridization between TM *d* orbitals (primarily $d_{\{xz\}}$, $d_{\{yz\}}$, $d_{\{xy\}}$) and host C-*p_z*, N-*p*, and F-*p* states near $E_{\rm F}$. In C₂N, covalent overlap with N-*p* dominates, broadening TM *d* states and stabilizing magnetism. In C₂CF, additional F-*p* contributions shift states and enhance ionic character, slightly quenching moments. This hybridization satisfies the Stoner criterion and is responsible for the observed spin-polarized metallicity.

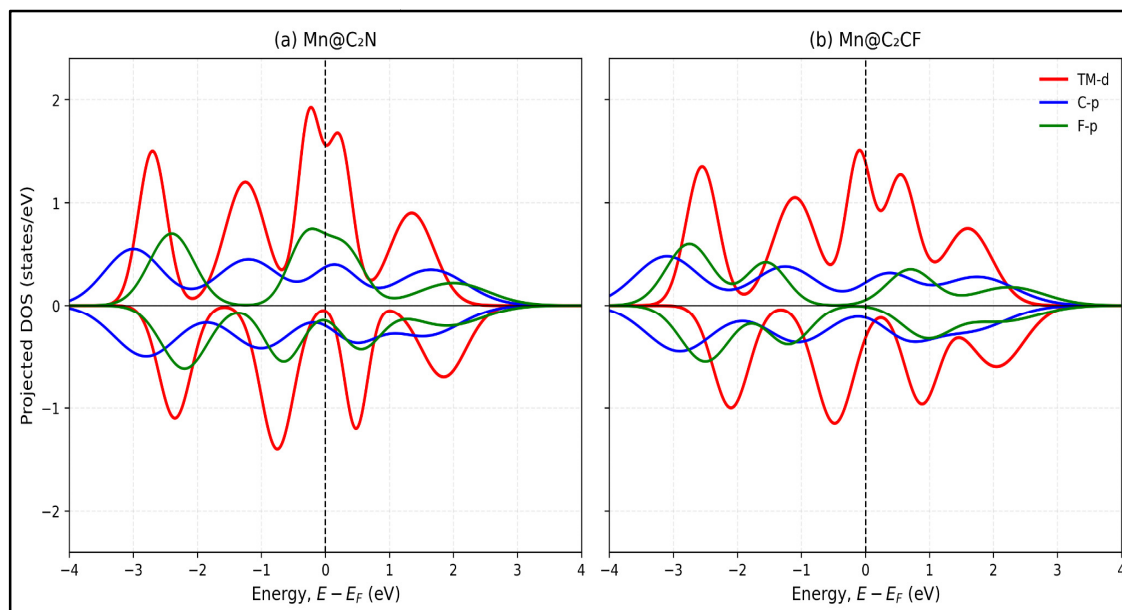


Figure 5: PDOS for (a) Mn embedded in C_2N and (b) Mn embedded in C_2CF showing TM- d (red), C- p (blue), N- p /F- p (green) contributions.

3.6 Charge Transfer and Spin-Density Localization

Bader charge analysis (Table 2) indicates unidirectional electron transfer from TM to host (0.65–1.55 $|e|$), more pronounced in C_2CF due to F electronegativity. Spin-density isosurfaces (Figure 6) for high-moment systems (e.g., Cr embedded in C_2N , Mn embedded in C_2CF) show primary localization on TM d orbitals with minor tails on adjacent atoms, confirming substrate-mediated polarization without long-range magnetic ordering in the dilute limit.

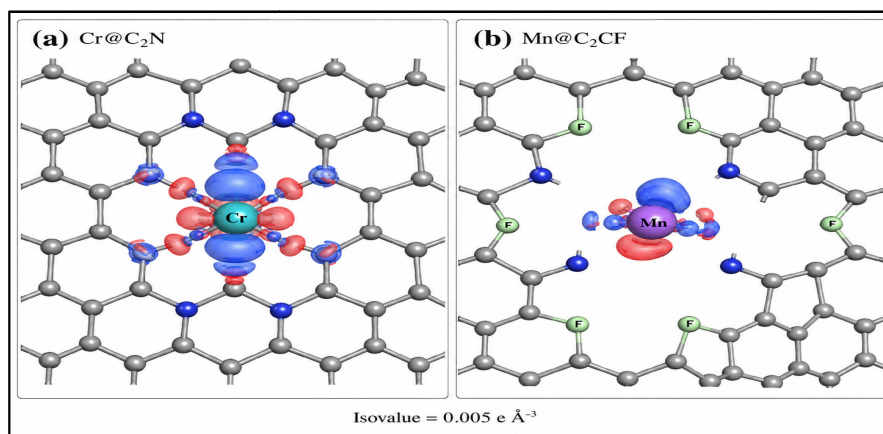


Figure 6: Spin-density maps (isovalue $0.005 \text{ e } \text{\AA}^{-3}$; blue = up, red = down) for Cr embedded in C_2N and Mn embedded in C_2CF .

Spin-density maps of Cr embedded in C₂N and Mn embedded in C₂CF show the spatial distribution of spin-up and spin-down charge densities at an isovalue of 0.005 e Å⁻³. Blue and red isosurfaces represent opposite spin channels. In Cr embedded in C₂N, the spin density is strongly centred on the Cr atom, with noticeable delocalisation toward neighbouring C/N atoms, indicating strong d–p hybridisation through the N-coordinated pore. In Mn embedded in C₂CF, the spin density remains mainly localised around Mn, with comparatively weaker host delocalisation, reflecting the more ionic and fluorine-modified pore environment of C₂CF.

3.7 Comparative Discussion: Why C₂N Binds Differently from C₂CF

The contrasting behavior originates from pore chemistry: C₂N's pyridinic N lone pairs enable strong covalent dative bonding and larger pore flexibility, yielding higher $|E_{ads}|$, delocalized moments, and robust hybridization. C₂CF's C–F substitution introduces higher electronegativity, pore contraction, and ionic character, leading to weaker adsorption, greater charge transfer, and modestly quenched/localized magnetism. These differences allow host-dependent tunability of magnetic and electronic properties.

3.8 Spintronic and Catalytic Relevance

The induced spin-polarized metallic/half-metallic states, tunable moments, and strong TM anchoring position TM embedded in C₂N and TM embedded in C₂CF as promising platforms for spin valves, magnetic sensors, and single-atom catalysts (e.g., ORR, CO₂ reduction). External electric fields or strain—building on prior bilayer graphene adatom studies—can further modulate these properties. Experimental realization via bottom-up synthesis or post-functionalization is highly feasible given the calculated stabilities.

4. Conclusion

In summary, spin-polarized density functional theory calculations demonstrate that adsorption of C₂N and C₂CF monolayers with 3d transition-metal atoms (Sc–Ni) provides a robust and tunable route to induce sizable local magnetic moments and spin-polarized metallic or half-metallic electronic states. All TM atoms preferentially anchor at the pore-centered sites, forming highly stable complexes with exothermic adsorption energies ranging from –3.85 to –5.68 eV on C₂N and –2.45 to –4.12 eV on C₂CF. The resulting magnetic moments vary systematically across the 3d series (0.6–3.8 μ_B on C₂N; 0.5–3.3 μ_B on

C₂CF), accompanied by strong *d*–*p* hybridization that closes the pristine band gaps and introduces spin-split bands crossing the Fermi level.

A central finding of this work is the distinctly different behavior of the two hosts, which originates from their contrasting pore chemistry and orbital environments. C₂N, with its six pyridinic nitrogen atoms lining the N₆ cavity, offers superior anchoring through strong covalent dative N-coordination. This leads to higher adsorption energies, slightly larger magnetic moments, more delocalized spin density, and robust half-metallic character in select systems (Ti, Cr, Co). In contrast, substitution of N by C–F units in C₂CF introduces fluorine-induced polarity, pore contraction, and a shift toward more ionic TM–F interactions. Consequently, C₂CF exhibits moderately weaker binding, enhanced charge transfer (by 0.2–0.4 *le*), and a tendency toward more localized magnetic moments with complete metallic character in both spin channels. These differences highlight how subtle chemical modification of the pore environment can serve as an effective design parameter for tailoring magnetic and electronic properties.

The present results significantly extend previous investigations of Fe and Co adatoms on bilayer graphene, where magnetic moments of ~2.3–2.8 μ_B and spin-split states near E_{F} were reported. By moving to porous frameworks, we achieve not only stronger single-atom stabilization but also greater tunability of spin-polarized transport—key requirements for practical spintronic devices such as spin valves, magnetic sensors, and spin filters. Additionally, the strong TM anchoring and exposed *d*-states position TM embedded in C₂N and TM embedded in C₂CF as promising single-atom catalysts for reactions such as CO₂ reduction and oxygen reduction, where the host-dependent charge transfer can modulate catalytic activity and selectivity.

Overall, this study establishes C₂N and C₂CF as versatile graphene-derived platforms for engineering magnetism and spin-polarized states through a combination of single-atom adsorption and pore chemistry modification. The computational insights provide a clear roadmap for experimental synthesis via bottom-up polymerization or post-synthetic metalation and for further property modulation via external electric fields, strain, or co-adsorption.

References:

- [1] K. S. Novoselov *et al.*, “Electric field effect in atomically thin carbon films,” *Science*, vol. 306, no. 5696, pp. 666–669, 2004, doi: [10.1126/science.1102896](https://doi.org/10.1126/science.1102896).
- [2] K. S. Novoselov *et al.*, “Two-dimensional gas of massless Dirac fermions in graphene,” *Nature*, vol. 438, pp. 197–200, 2005, doi: [10.1038/nature04233](https://doi.org/10.1038/nature04233).
- [3] A. H. Castro Neto, F. Guinea, N. M. R. Peres, K. S. Novoselov, and A. K. Geim, “The electronic properties of graphene,” *Reviews of Modern Physics*, vol. 81, no. 1, pp. 109–162, 2009, doi: [10.1103/RevModPhys.81.109](https://doi.org/10.1103/RevModPhys.81.109).
- [4] W. Han, R. K. Kawakami, M. Gmitra, and J. Fabian, “Graphene spintronics,” *Nature Nanotechnology*, vol. 9, no. 10, pp. 794–807, 2014, doi: [10.1038/nnano.2014.214](https://doi.org/10.1038/nnano.2014.214).
- [5] O. V. Yazyev, “Emergence of magnetism in graphene materials and nanostructures,” *Reports on Progress in Physics*, vol. 73, no. 5, Art. no. 056501, 2010, doi: [10.1088/0034-4885/73/5/056501](https://doi.org/10.1088/0034-4885/73/5/056501).
- [6] B. Uchoa, T. G. Rappoport, and A. H. Castro Neto, “Localized magnetic states in graphene,” *Physical Review Letters*, vol. 101, no. 2, Art. no. 026805, 2008, doi: [10.1103/PhysRevLett.101.026805](https://doi.org/10.1103/PhysRevLett.101.026805).
- [7] H. Valencia, A. Gil, and G. Frapper, “Trends in the adsorption of 3d transition metal atoms onto graphene and nanotube surfaces: A DFT study and molecular orbital analysis,” *The Journal of Physical Chemistry C*, vol. 114, no. 33, pp. 14141–14153, 2010, doi: [10.1021/jp103445v](https://doi.org/10.1021/jp103445v).
- [8] M. Manadé, F. Viñes, and F. Illas, “Transition metal adatoms on graphene: A systematic density functional study,” *Carbon*, vol. 95, pp. 525–534, 2015, doi: [10.1016/j.carbon.2015.08.072](https://doi.org/10.1016/j.carbon.2015.08.072).
- [9] J. Mahmood *et al.*, “Nitrogenated holey two-dimensional structures,” *Nature Communications*, vol. 6, Art. no. 6486, 2015, doi: [10.1038/ncomms7486](https://doi.org/10.1038/ncomms7486).
- [10] J. Du, C. Xia, W. Xiong, X. Zhao, T. Wang, and Y. Jia, “Tuning the electronic structures and magnetism of two-dimensional porous C₂N via transition metal embedding,” *Physical Chemistry Chemical Physics*, vol. 18, no. 32, pp. 22678–22686, 2016, doi: [10.1039/C6CP03210A](https://doi.org/10.1039/C6CP03210A).

- [11] S. Gong *et al.*, “Tunable half-metallic magnetism in an atom-thin holey two-dimensional C₂N monolayer,” *Journal of Materials Chemistry C*, vol. 5, no. 33, pp. 8424–8430, 2017, doi: [10.1039/C7TC01399J](https://doi.org/10.1039/C7TC01399J).
- [12] J. Du, C. Xia, W. Xiong, X. Zhao, T. Wang, and Y. Jia, “Tuning the electronic structures and magnetism of two-dimensional porous C₂N via transition metal embedding,” *Physical Chemistry Chemical Physics*, vol. 18, no. 32, pp. 22678–22686, 2016, doi: [10.1039/C6CP03210A](https://doi.org/10.1039/C6CP03210A).
- [13] Q. Bing, W. Liu, W. Yi, and J. Liu, “Ni anchored C₂N monolayers as low-cost and efficient catalysts for hydrogen production from formic acid,” *Journal of Power Sources*, vol. 413, pp. 399–407, 2019, doi: [10.1016/j.jpowsour.2018.12.063](https://doi.org/10.1016/j.jpowsour.2018.12.063).
- [14] S. Khan *et al.*, “Transition-metal single atom catalyst embedded in C₂N for toxic-gas reduction reaction and selective gas-sensing application: Atomic-scale study,” *Applied Surface Science*, vol. 589, Art. no. 152916, 2022, doi: [10.1016/j.apsusc.2022.152916](https://doi.org/10.1016/j.apsusc.2022.152916).
- [15] H.-J. Kim and J.-H. Cho, “Fluorine-induced local magnetic moment in graphene: A hybrid DFT study,” *Physical Review B*, vol. 87, no. 17, Art. no. 174435, 2013, doi: [10.1103/PhysRevB.87.174435](https://doi.org/10.1103/PhysRevB.87.174435).
- [16] A. M. Schrier, “Fluorinated graphene: A theoretical study,” *ACS Nano*, vol. 4, no. 11, pp. 6813–6820, 2010, doi: [10.1021/nn101550n](https://doi.org/10.1021/nn101550n).
- [17] H.-J. Kim and J.-H. Cho, “Fluorine-induced local magnetic moment in graphene: A hybrid DFT study,” *Physical Review B*, vol. 87, no. 17, Art. no. 174435, 2013, doi: [10.1103/PhysRevB.87.174435](https://doi.org/10.1103/PhysRevB.87.174435).
- [18] D. Nafday, T. Saha-Dasgupta, and D. D. Sarma, “Magnetism of an adatom on bilayer graphene and its control: A first-principles perspective,” *Physical Review B*, vol. 88, no. 20, Art. no. 205422, 2013, doi: [10.1103/PhysRevB.88.205422](https://doi.org/10.1103/PhysRevB.88.205422).
- [19] G. Kresse and J. Hafner, “Ab initio molecular dynamics for liquid metals,” *Physical Review B*, vol. 47, no. 1, pp. 558–561, 1993, doi: [10.1103/PhysRevB.47.558](https://doi.org/10.1103/PhysRevB.47.558).
- [20] G. Kresse and J. Furthmüller, “Efficient iterative schemes for ab initio total-energy calculations using a plane-wave basis set,” *Physical Review B*, vol. 54, no. 16, pp. 11169–11186, 1996, doi: [10.1103/PhysRevB.54.11169](https://doi.org/10.1103/PhysRevB.54.11169).
- [21] P. E. Blöchl, “Projector augmented-wave method,” *Physical Review B*, vol. 50, no. 24, pp. 17953–17979, 1994, doi: [10.1103/PhysRevB.50.17953](https://doi.org/10.1103/PhysRevB.50.17953).

- [22] J. P. Perdew, K. Burke, and M. Ernzerhof, “Generalized gradient approximation made simple,” *Physical Review Letters*, vol. 77, no. 18, pp. 3865–3868, 1996, doi: [10.1103/PhysRevLett.77.3865](https://doi.org/10.1103/PhysRevLett.77.3865).
- [23] S. Grimme, J. Antony, S. Ehrlich, and H. Krieg, “A consistent and accurate ab initio parametrization of density functional dispersion correction (DFT-D) for the 94 elements H–Pu,” *The Journal of Chemical Physics*, vol. 132, no. 15, Art. no. 154104, 2010, doi: [10.1063/1.3382344](https://doi.org/10.1063/1.3382344).
- [24] J. Mahmood *et al.*, “Nitrogenated holey two-dimensional structures,” *Nature Communications*, vol. 6, Art. no. 6486, 2015, doi: [10.1038/ncomms7486](https://doi.org/10.1038/ncomms7486).
- [25] G. Henkelman, A. Arnaldsson, and H. Jónsson, “A fast and robust algorithm for Bader decomposition of charge density,” *Computational Materials Science*, vol. 36, no. 3, pp. 354–360, 2006, doi: [10.1016/j.commatsci.2005.04.010](https://doi.org/10.1016/j.commatsci.2005.04.010).
- [26] V. Wang, N. Xu, J.-C. Liu, G. Tang, and W.-T. Geng, “VASPKIT: A user-friendly interface facilitating high-throughput computing and analysis using VASP code,” *Computer Physics Communications*, vol. 267, Art. no. 108033, 2021, doi: [10.1016/j.cpc.2021.108033](https://doi.org/10.1016/j.cpc.2021.108033).
- [27] K. Momma and F. Izumi, “VESTA 3 for three-dimensional visualization of crystal, volumetric and morphology data,” *Journal of Applied Crystallography*, vol. 44, no. 6, pp. 1272–1276, 2011, doi: [10.1107/S0021889811038970](https://doi.org/10.1107/S0021889811038970).